Observation of Fracture Sealing in High-strength and Ultra-low-permeability Concrete by Micro-focus X-ray CT and SEM/EDX

Daisuke FUKUDA[1], Megumi MARUYAMA[2], Yoshitaka NARA[3], Daisuke HAYASHI[4,5], Hideo OGAWA[4], Katsuhiko KANEKO[1,6]

[1] *Faculty of Engineering, Hokkaido University, Kita 13 Nishi 8, Kita-ku, Sapporo, Hokkaido 060-8628, Japan*

[2] *Graduate School of Engineering, Hokkaido University, Kita 13 Nishi 8, Kita-ku, Sapporo, Hokkaido 060-8628, Japan*

[3] *Graduate School of Engineering, Tottori University, 4-101 Koyama-Minami, Tottori 680-8552, Japan*

[4] *Taiheiyo Consultant Co., Ltd., Ohsaku, Sakura, Chiba 285-8655, Japan*

[5] *Radioactive Waste Management Funding and Research Center, 1-15-7, Tsukishima, Chuo-ku, Tokyo 104-0052, Japan*

[6] *Horonobe Research Institute for Subsurface Environment, 5-3 Sakaemachi, Horonobe-cho, Teshio-gun, Hokkaido 098-3221, Japan*

*Corresponding author: Daisuke FUKUDA

E-mail: d-fukuda@frontier.hokudai.ac.jp

Tel/Fax: +81-11-706-6302

Abstract

Fracture sealing by precipitation is known to occur in high-strength and ultra-low-permeability concrete (HSULPC) immersed in water. Because a high ability to retard radionuclide migration is required for HSULPC, understanding both the sealing process and the composition of sealing deposits is important to identify optimum conditions for significant sealing. In this study, sealing of a macro-fractured HSULPC specimen with initial aperture of approximately 0.1 mm was investigated in simulated seawater over 49 days. The composition of sealing deposits at 49 days after immersion was clarified by scanning electron microscopy and energy dispersive X-ray spectroscopy (SEM/EDX), and the progress of sealing during the 49 days was clarified by image analysis with micro-focus X-ray computed tomography (X-rayCT). Both the SEM/EDX and X-rayCT results showed that significant sealing was attained only near the outermost part of the specimen. The SEM/EDX results showed that a thin brucite layer formed on the entire specimen surface over which significant precipitation of calcium carbonate occurred and sealed the macro-fracture only near the outermost part of the specimen. The X-rayCT results indicated that the amount of sealing deposits in the macro-fracture (P_{seal}) reached 70 % in the mostly sealed region at 49 days and the rate of change in P_{seal} became maximum (3.7 % day^{-1}) during 7–21 days after immersion, then decreased. In conclusion,

the findings in this study represent an important clue in the search for optimum conditions to achieve fracture sealing in HSUPLC.

Keywords: Self-sealing, Micro-focus X-ray CT, SEM, EDX, 3-D image registration, High-strength and ultra-low-permeability concrete, Radioactive waste disposal

1. Introduction

For the geological disposal of radioactive waste, the radioactive intensity of radionuclides can be reduced by the combination of both engineered barriers such as bentonite buffers and natural barriers such as rock mass. If a repository of radioactive waste is located in an area of high hydraulic gradient and large permeability, the retardation of radionuclide migration by these barriers may not be sufficient. To retard radionuclide migration, several alternative concepts of radioactive waste packages have been developed. For instance, high-strength and ultra-low-permeability concrete (HSULPC) is planned for radioactive waste and the geological disposal of transuranic (TRU) waste (Kawasaki et al. 2005; Owada et al. 2005; Shibuya et al. 2005) to confine radionuclides with low adsorption in engineered barriers, such as ^{14}C, which is included in Japanese TRU waste.

In general, water migrates through networks of fractures and pores in a solid. The formation of calcium carbonate or calcium hydroxide on the surfaces of fractures and pores by such water migration in cementitious composites and cementitious materials has been reported (e.g., Wu et al. 2012). For concrete of sufficient age, the formation of calcium carbonate primarily occurs (e.g. Jacobsen and Sellevold 1996; Hearn and Morley 1997; Hearn 1997; Edvardsen 1999;Van der Zwaag 2007; Homma et al. 2009; Qian et al. 2009; Yang et al. 2009). While Heap et al. (2013) showed that the water permeability of concrete increases significantly with the progress of fracturing, it is also possible that the sealing of existing fractures and pores affects the permeability of concrete. So far, various reports on the fracture sealing of concrete have been published (e.g., Jacobsen and Sellevold 1996; Hearn and Morley 1997; Hearn 1997; Edvardsen 1999; Reinhardt and Jooss 2003; Granger et al. 2007; Van der Zwaag 2007; Homma et al. 2009; Qian et al. 2009; Yang et al. 2009; Ahn and Kishi 2010; Wu et al. 2012; Fukuda et al. 2012; Fukuda et al. 2013). Among this literature, Edvardsen (1999) showed that the sealing of a fracture occurs by the precipitation of calcium carbonate, generated from CO_3^{2-} in the water and Ca^{2+} in the cement paste, and that the fracture aperture and applied water pressure significantly affect the sealing, while the types of cement and aggregate and the hardness of the water have no influence on the sealing rate. Reinhardt and Jooss (2003) showed that fracture sealing is significantly influenced by temperature up to 80 °C, resulting in a decrease in water transport, i.e., more significant sealing with increasing temperature. It has been shown that sealing in engineered cementitious composites in water occurs if the fracture aperture is less than 0.15 mm (Yang et al. 2009), while sealing in HSULPC kept in simulated seawater up to 49 days occurred when the fracture aperture was 0.1 mm but not 0.25 mm (Fukuda et al. 2012; Fukuda et al. 2013). Thus, it seems that not only the composition of cementitious composites and cementitious materials and its spatial distribution but also the surrounding environment affect sealing behavior. Furthermore, fracture sealing has also been observed in various rocks (e.g., Fisher and Brantley 1992; Gratier et al. 1994; Evans and Chester 1995; Tsang et al. 2005).

Because a high ability to retard radionuclide migration is required for HSULPC, detailed investigation of the sealing of fractures and pores in HSULPC in various surrounding environments (e.g. water type, temperature, water pressure) is of paramount importance. So far, micro X-ray computed tomography (X-rayCT) coupled with image analysis has been applied to concrete, limestone, and sandstone samples before and after bacterial weathering (Graef et al. 2005). Micro X-rayCT has also been applied to evaluate the 3-D porosity distribution of partly calcium leached cement paste (Wan et al. 2013). From these applications, micro X-rayCT has been shown to be an effective tool to 3-dimensionally observe and evaluate the microstructure of such materials in a nondestructive manner. However, only a few studies have applied micro X-rayCT to analyze HSULPC. Thus, Fukuda et al. (2012; 2013) applied both micro-focus X-rayCT and 3-D image analysis to investigate the sealing process in HSULPC. Specifically, the sealing of macro-fractured HSULPC specimens with initial fracture aperture of approximately 0.10 mm and 0.25 mm were investigated by holding the specimens in simulated seawater for up to 49 days. Significant precipitation occurred over approximately 0.3 mm only near the outermost parts of the fractured surface in the specimen, regardless of the target fracture aperture, and significant sealing was only achieved in the case of a fracture aperture of 0.10 mm. However, the detailed composition of sealing deposits on the fracture surface of HSULPC cannot be clarified only by X-rayCT. If the composition of sealing deposits can be clarified, the knowledge can be utilized to find optimum conditions and new techniques to accelerate precipitation and fracture sealing.

Considering the above background, we investigate the sealing of macro-fractures in HSULPC immersed in simulated seawater for up to 49 days using scanning electron microscopy and energy dispersive X-ray spectroscopy (SEM/EDX) to identify the detailed configuration and composition of sealing deposits, as well as using micro-focus X-rayCT. In addition, because the volume of the region quantitatively analyzed by X-rayCT image analysis was quite small relative to that of the significantly sealed region analyzed in Fukuda et al. (2012), temporal changes in the amount of sealing deposits in a much broader region were evaluated by micro-focus X-rayCT image analysis to elucidate the sealing process in more detail.

2. Sample preparation

HSULPC made by Taiheiyo Consultant Co., Ltd., Sakura, Japan, was used. While detailed information on the HSULPC specimen can be found in Kawasaki et al. (2005), Nara et al. (2010) and Fukuda et al. (2012; 2013), brief details are presented here for completeness. The composition of the HSULPC specimen is shown in Table 1 (Fukuda et al. 2012; 2013). The specimen was prepared such that its composition of low-heat Portland cement, silica fume, fillers, and aggregates totaled 2300 kg/m^3, with the amount of each component within the range listed in the table. The procedure used to prepare the HSULPC was based on the recommendation proposed by the Japan Society of Civil Engineers (2004). The porosity of the HSULPC as measured by mercury porosimetry was 5 % (Kawasaki et al. 2005). The hydraulic conductivity was 4×10^{-19} m/s (Kawasaki et al. 2005).

The sample used in this study was prepared in the following way. An initially intact cylindrical HSULPC specimen with diameter and height of approximately 13 and 15 mm, respectively, was split in half axially using a diametrical compression test (also known as diametrical tensile test, Brazilian disk test, indirect tensile test, compact crushing test, or compact hardness test) (e.g., Hondros 1959; International Society for Rock Mechanics 1978), and was set in an approximately 35-mm-high acrylic cylinder tube using epoxy glue. To keep the induced fracture (hereafter, this fracture is called “macro-fracture”) open between each macro-fracture surface, a thin polytetrafluoroethylene (PTFE) sheet with a thickness of 0.10 mm was inserted. Consequently, the initial width of the macro-fracture in the specimen was approximately 0.10 mm. The age of the HSULPC specimen used in this study was approximately two years. Because salt water is often found underground (Mizukami et al. 1977; Iwatsuki et al. 2005; Hama et al. 2007), the HSULPC specimen was kept in simulated seawater based on the groundwater conditions in Japan (chemical composition in Table 2). The sealing of the macro-fracture was observed using micro-focus X-rayCT (Fukuda et al. 2012). The precipitated region was found to increase over the 49 days and precipitation was observed approximately 0.3 mm from the outermost part of the macro-fracture surface of the specimen as shown in in Fig. 1 (hereafter, this outermost part is just called the “end”).

The sealed HSULPC specimen was also studied using SEM/EDX. Prior to analysis, the macro-fracture was filled with epoxy resin, and the specimen was then cut through two different planes as shown in Fig.1. The cut planes were ground in the direction parallel to the axis of the cylinder to allow observation of the precipitates on the macro-fracture at different depths, as shown in Fig. 2.

3. Observation by SEM/EDX

3.1. Observation Method

A SHIMADZU SUPERSCAN SS-550 (Shimadzu Corporation, Kyoto, Japan) SEM/EDX installed at Hokkaido University, Japan, was used to observe the precipitates on the macro-fracture at different depths, i.e., from the end to the interior of the specimen. Before observation, carbon was deposited on the specimen surfaces as shown in Fig. 2 to avoid the serious image distortion or drift due to charging of the specimen surface (e.g., Reed 2010). Secondary electron images of the precipitates were observed by SEM, and the chemical components of the precipitates formed on the macro-fracture surface were identified by EDX mapping.

3.2. Results

Figure 3 shows an SEM image of one end of the specimen where significant sealing occurred. In the figure, acicular precipitates clearly filled and sealed the macro-fracture over an area approximately 80–90 μm from the end to the interior of the specimen. As shown in Fig. 4, such 50-μm-thick acicular precipitates were also observed over the wider area of the surface end of the specimen. Similar precipitation and sealing by the acicular precipitates were observed at the other end of the specimen. This behavior agrees well with that previously observed using X-rayCT (Fukuda et al. 2012). In contrast, Fig. 5 shows an SEM image of a macro-fracture in the interior of the specimen. Note that the macro-fracture is locally bifurcated in the figure. Triangular precipitates with a scale of a few micrometers were found to have occurred on the fracture surface. These minute precipitates were observed over the entire fracture surface of the specimen. However, sealing by the triangular precipitates occurred only in extremely local areas of the surface of the macro-fracture where the fracture aperture was much smaller than 0.1 mm. Because their sizes were smaller than the resolution of micro-focus X-rayCT, these precipitates were not identified in the CT observations. From these SEM observations, it is reasonable to assume that the sealing of macro-fractures near the end of the specimen was caused by the aforementioned acicular precipitates.

For the detailed chemical composition of the precipitates, Figs. 6, 7, and 8 show SEM images with the corresponding concentration distributions of Ca, Mg, C, Si, and O identified by EDX mapping for the regions shown in Figs. 3, 4, and 5, respectively. In these figures, the very large concentration of C in some regions corresponds to the aforementioned epoxy resin and carbon deposition. Figure 6 shows that the sealing deposits mainly consisted of Ca, C and O. This type of precipitation was also found in Fig. 7 on the surface end of the specimen. However, as shown in Fig. 8, this type of precipitate was not observed on the macro-fracture surface in the interior of the specimen. In addition, Figs. 6, 7, and 8 also show that the precipitation containing Mg occurred on the entire surface of the specimen, including the macro-fracture surface.

3.3. Discussion

Considering that Ca, C, and O were predominantly observed around the sealed region, the main composition of the sealing deposits was likely calcium carbonate. In addition, because the SEM observation showed that the shape of the precipitates was acicular and because it has been reported that typical concrete exposed to seawater may develop a surface skin consisting of a layer of magnesium hydroxide (brucite) overlain by a more slowly developing layer of aragonite (Buenfeld and Newman, 1986), the calcium carbonate formed may have been aragonite.

The precipitates containing Mg were expected to be brucite or dolomite, because they covered the entire surface of the specimen and because O component was also observed in the region where Mg component. Considering previous works studying precipitation on concrete surfaces in seawater (e.g., Buenfeld and Newman, 1986), and because carbonate ions could not be supplied to the system under the tested conditions and the dissolved carbonate ions were expected to be used in the precipitation of aforementioned calcium carbonate, these precipitates should be brucite.

From the above discussion and considering that the HSULPC specimen used in this study was sufficiently old, i.e. approximately 2 years, the primary mechanism for the sealing of macro-fractures near the end of the specimen under the tested conditions is the deposition of calcium carbonate (aragonite) over the layer of brucite. Because calcium carbonate was not observed on the macro-fracture in the interior of the specimen, the supply of dissolved carbonate ions was only possible around the end surface of the specimen and macro-fractures in the vicinity of the outermost end of the specimen. We infer that the fracture may be sealed only by brucite if the fracture aperture is much smaller than 0.1 mm.

4. Evaluation of sealing by X-rayCT image analysis

The SEM/EDX observation showed that significant sealing occurred by precipitation of calcium carbonate over a brucite layer only near the end of the specimen at 49 days immersion in simulated seawater. However, the temporal change in the amount of sealing deposits cannot be understood only with SEM/EDX. Thus, we considered that coupling the SEM results with micro-focus X-rayCT image analysis would result in better understanding of fracture sealing. In addition, the temporal change in the amount of sealing deposits in the most significantly sealed region of the macro-fracture was not evaluated in the X-rayCT image analysis by Fukuda et al. (2012), i.e., the region approximately 0.1 mm from the outermost end of the specimen was excluded from the region of analysis. Because the resolution of SEM is higher than that of micro-focus X-rayCT, the SEM results could also be used to verify the precision of the X-rayCT image analysis results.

This work extended the region of analysis into a much wider area, i.e. toward the most significantly sealed region of the specimen. The results of X-rayCT image analysis results were verified by comparison with the SEM observations, and the temporal change in the amount of sealing deposits was then evaluated in detail.

4.1. Image analysis Method

To investigate the temporal changes in the precipitated regions of the macro-fracture, it is necessary to extract the corresponding regions using image analysis. This study basically followed the image analysis method explained by Fukuda et al. (2012), i.e., the extraction of the precipitated region by image subtraction of the X-rayCT images obtained before and after the specimen was immersed in simulated seawater, based on image registration by 3-D affine transform with 12 unknown coefficients. The analysis was applied to the region of interest (ROI) shown in Fig. 9. The shape of the ROI was a rectangular parallelepiped with a length of 6.4 mm, width of 4.3 mm, and height of 1.4 mm from the X-rayCT image corresponding to the outermost end of the specimen. The top part of the ROI over 0.1 mm in the height direction is a newly evaluated region in this study for which the coefficients for the affine transform need to be adequately determined. Those for 0.3 mm from this region to the interior of the ROI were previously obtained by Fukuda et al. (2012). From our preliminary investigation, the unknown coefficients were found to approximate to constant values throughout the specimen and thus the previously identified coefficients for affine transform reported by Fukuda et al. (2012) were used throughout the entire ROI for the 3-D image registration. Then, by subtracting the gray values of the CT images obtained before immersion from those obtained after immersion water, only the precipitated regions were extracted in the subtraction images.

4.2. Results

Figure 10 shows the results of 3-D image subtraction images binarized by the threshold value determined through a maximum likelihood thresholding method (Kitamoto 1999; Kitamoto and Takagi 1999; Kato et al. 2013; Kato et al. 2014) that considered the partial volume effect (e.g., Kecham and Carson 2001), i.e., the effect of mixels (mixed pixels) (Choi et al. 1991). Fig. 10 (a), (b), and (c) correspond to the binarized subtraction images obtained before and after the specimen was immersed in simulated seawater for 7 days, 21 days, and 49 days, respectively. In these figures, only the precipitated regions are displayed (in white). From these results, the progress of the increase in the amount of precipitation with immersion time was successfully extracted with minor noise. In Fig. 10 (c) in particular, the regions of precipitation in the macro-fracture connected well with each other as well as the increase in the amount of precipitation on the surface end of the specimen.

To verify the results of the proposed image analysis, the precipitated regions in the binarized subtraction image in Fig. 10 (c) and the SEM image of the same cross-section in Fig. 3 were compared. Figure 11 shows the subtraction image of the same plane as that observed by SEM after immersion of the sample in simulated seawater for 49 days. This region is indicated by dash-dotted lines in Fig. 10 (c) and corresponds to the region observed in Fig. 3. In Fig. 11, the macro-fracture surface and contour of the specimen are indicated by dotted lines. It was found that the precipitation with a vertically long spherical shape sealed the macro-fracture over 3 voxels, i.e., 75 μm with our X-rayCT scanning conditions, in the depth direction.

4.3. Discussion

By comparing the overall shape and thicknesses of the sealed region identified by SEM, i.e., approximately 80–90 μm, with that obtained by the X-rayCT image analysis, i.e., 75 μm, it was found that the thicknesses evaluated by these two approaches roughly showed good agreement with each other. Because the SEM image had a higher spatial resolution than the X-rayCT image, the thickness of the sealed region measured by SEM must be slightly larger than that evaluated from X-rayCT image, considering both the applied X-rayCT image resolution, i.e., 16 × 16 × 25 μm and a partial volume effect between the precipitated and non-precipitated regions. As a result, it can be concluded that our X-rayCT image analysis was able to reasonably extract and evaluate the sealed region. It is also noted that, if a X-rayCT scanner with higher resolution than that applied in this research were available a much better agreement between the SEM and X-rayCT image analysis results would be attainable.

Because the proposed X-rayCT image analysis technique is now able to evaluate the temporal change in the amount of sealing deposits in the macro-fracture including the region that Fukuda et al. (2012) was not able to evaluate, the binarized subtraction images in Fig. 10 were analyzed in detail. For this purpose, both the percentage of sealing deposits in the macro-fracture denoted as P_{seal} (%), and the temporal changes in P_{seal}, denoted as R_{seal} (% day^{-1}) were calculated using the following equations:

$$P_{\mathrm{seal}} = \frac{V_{\mathrm{pre}}}{V_{\mathrm{fract}}} \times 100(\%) \quad (1)$$

$$R_{\mathrm{seal}} = \frac{\Delta P_{\mathrm{seal}}}{\Delta t}\left(\% \cdot \mathrm{day}^{-1}\right) \quad (2)$$

where V_{pre} (μm^3) is the total volume of precipitate in the ROI and V_{fract} (μm^3) is the total volume of the macro-fracture in the ROI, both of which are calculated by simply counting the number of voxels corresponding to precipitate and macro-fracture, respectively, and ΔP_{seal} (%) is the change in P_{seal} over a given immersion period, Δt (day). The voxel size was 16 × 16 × 25 μm. It may be noted that the definition of Eq. (1) is slightly different from that used by Fukuda et al. (2012; 2013) in which P_{seal} was calculated for the region where the fracture aperture could be considered almost constant. Because the fracture aperture in the ROI analyzed in this study cannot be considered to be constant, the definition of P_{seal} in Eq. (1) was used instead.

Figure 12 shows P_{seal} with respect to the depth, h (mm), from the outermost side to the interior of the ROI. In each period, P_{seal} increased drastically towards the end, and P_{seal} for h = 0–0.3 mm increased with elapsed time where the maximum value of P_{seal}, almost 70 %, was attained at h = 0. In particular, the gradient of P_{seal} for h = 0–0.1 mm, where significant precipitation of calcium carbonate and brucite occurred, is clearly larger than that for h = 0.1–0.3 mm, where only precipitation of brucite occurred.

Figure 13 shows R_{seal} with respect to the depth, h (mm), from the outermost side to the interior of the ROI. In Fig. 13, Δt was 7 days if the specimen was taken out of the water 7 days after immersion. Similarly, Δt was 14 (or 28) days if the specimen was placed in water at 7 (or 21) days and taken out of the water at 21 days (or 49 days), respectively. It was found that R_{seal} at each period attained a maximum value at the top of the ROI (h = 0) and monotonically decreased toward the interior of the specimen. It was also found that the change in R_{seal} with respect to h near the top of the ROI (approximately h = 0–0.1 mm) was much larger than that in the interior of the specimen (approximately h = 0.1–0.3 mm). Especially for R_{seal} at h = 0, which was relatively large in value at 3.5 % day^{-1} during 0–7 days, slightly increased to 3.7 % day^{-1} during 7–21 days, the largest R_{seal} observed during the entire immersion period, and then decreased to 2.5 % day^{-1} during 21–49 days. In addition, $R_{\mathrm{seal}} > 0$ was found over h = 0–0.2 mm during 0–7 days and over h = 0–0.3 mm during 7–21 days, followed by slight increase in the range of $R_{\mathrm{seal}} > 0$ during 21–49 days.

Because significant precipitation of calcium carbonate overlain by brucite was only observed near the top of the ROI (approximately over h = 0–0.1 mm), the relatively larger P_{seal} and R_{seal} near the top of ROI may be due to precipitation of calcium carbonate and brucite, and the relatively smaller P_{seal} and R_{seal} in the interior purely reflect the precipitation of brucite. We infer that the macro-fracture in the vicinity of the end of the specimen was in an environment where the precipitation of calcium carbonate was enhanced by sufficient supply of carbonate ions from the simulated seawater in the period up to approximately 21 days. Because a decrease in R_{seal} was observed at h = 0–0.1 mm after 21 days and available space for precipitation of calcium carbonate at the same h also decreased with time, the progress of significant sealing from the top end could limit the supply of carbonate ions to the interior of the specimen. This could result in the lower precipitation of calcium carbonate toward the interior of the specimen and the isolation of macro-fracture in the interior of the specimen. With these considerations, we expect that R_{seal} for h = 0.1–0.3 mm would converge to zero if the specimen was kept in water longer, although R_{seal} in this region was greater than 0 during 21–49 days.

Considering the applications of HSULPC, it is desirable that such sealing should occur over a short period and toward the deeper region in the macro-fracture, and thus the identification of the environmental conditions such as water pressure and temperature are of paramount importance. To achieve this, the detailed mechanism of the aforementioned localized precipitation and sealing should be clarified. However, because the chemistry involving the surface of narrow fractures in heterogeneous concrete matrix can be extremely complex and require more comprehensive study, we regard this as future work.

5. Conclusion

In this study, the sealing of macro-fractured HSULPC specimen immersed in simulated seawater for up to 49 days was investigated using SEM/EDX and X-rayCT image analysis to identify the detailed configuration and composition of sealing deposits and to evaluate the temporal changes in the amount of sealing deposits, respectively. The important findings are as follows:

· Both the SEM and X-rayCT image analyses showed that significant precipitation occurred approximately 0.3 mm from each outermost end of the specimen, in which significant sealing was found over approximately 0.1 mm. The X-rayCT image analyses indicated that the percentage of sealing deposits in the macro-fracture reached almost 70 % in the mostly sealed region after immersion in simulated sweater for 49 days, while the rate of change in the percentage of sealing deposits in the macro-fracture reached almost 3.7 % day^{-1} during 7–21 days after immersion, then decreased. These evaluated values are much larger than those obtained in our previous work (Fukuda et al. 2012). In addition, the X-rayCT results were found to agree well with those of SEM analysis.

· SEM/EDX results indicated that the main component of the sealing deposits near each outermost end of the specimen in the macro-fracture was calcium carbonate (aragonite) overlaying a thin layer of brucite. In addition, precipitation of the layer of brucite was observed over the entire surface of the specimen, i.e., not limited to the fracture surface, and fracture sealing by brucite was also observed in extremely local regions where the fracture aperture became quite small. Therefore, if the fracture aperture is much smaller, i.e., possibly on the order of several micrometers, fractures even in the interior of the specimen may be sealed only by brucite.

· On the micrometer scale, the coupled approach of SEM with X-rayCT image analysis proposed in this study will be a useful tool for the quantitative evaluation of the sealing process when the resolution of the X-rayCT scanner improves.

· By coupling X-rayCT with surface-based quantification methods including SEM/EDX, detailed information about both the progress of sealing and resultant sealing deposits can be obtained for the same specimen, otherwise it is quite difficult to achieve and the necessity of the preparation of multiple specimens occurs, resulting in the compromise of reproducibility of the obtained results.

Acknowledgment

We appreciate the kind support and valuable advice of the Radioactive Waste Management Funding and Research Center, Tokyo, Japan.

References

Kawasaki T, Asano H, Owada H, Otsuki A, Yoshida T, Matsuo T, Shibuya K, Takei A (2005) Development of Waste Package for TRU-disposal (4)—Evaluation of Confinement Performance of TRU Waste Package Made of High-strength and Ultra Low-permeability Concrete. Proc. GLOBAL 2005, Tsukuba, Japan:254

Owada H, Otsuki A, Asano H (2005) Development of Waste Package for TRU-disposal (1)—Concepts and Performances. Proc. GLOBAL 2005, Tsukuba, Japan:351

Shibuya K, Asano H, Owada H, Otsuki A, Kawasaki T, Yoshida T, Matsuo T, Takei A (2005) Development of Waste Package for TRU-disposal (3)—Examination of Manufacturing Technique of TRU Waste Package Made of High-strength and Ultra Low-permeability Concrete. Proc. GLOBAL 2005, Tsukuba, Japan:256

Wu M, Johannesson B, Geiker M (2012) Review: Self-healing in Cementitious Materials and Engineered Cementitious Composite as A Self-healing. Material Constr Build Mater 28(1):571–583

Jacobsen S, Sellevold EJ (1996) Self healing of high strength concrete after deterioration by freeze/thaw. Cem Concr Res 26(1):55–62

Hearn N, Morley CT (1997) Self-sealing Property of Concrete—Experimental Evidence.

Mater Struct 30(201): 404–411

Hearn N (1997) Self-sealing, autogenous healing and continued hydration: What is the difference? Mater Struct 31(8):563–567

Edvardsen C (1999) Water permeability and autogenous healing of cracks in concrete. ACI Mater J 96(4):448–455

Reinhardt H, Jooss M (2003) Permeability and self-healing of cracked concrete as a function of temperature and crack width. Cem Concr Res 33(7):981–985

Van der Zwaag S (2007) Self-healing Materials: An Alternative Approach to 20 Centuries of Material Science (1st ed). Springer, USA.

Homma D, Mihashi H, Nishiwaki, T (2009) Self-healing Capability of Fibre Reinforced Cementitious Composites. J Adv Concr Technol 7(2):217–228

Qian S, Zhou J, de Rooij MR, Schlangen E, Ye G, van Breugel K (2009) Self-healing Behavior of Strain Hardening Cementitious Composites Incorporating Local Waste Materials. Cem Concr Compos 31(9):613–621

Yang Y, Lepech MD, Yang EH, Li VC (2009) Autogenous healing of engineered cementitious composites under wet-dry cycles. Cem Concr Res 39(5):382–390

Granger S, Loukili A, Pijaudier-Cabot G, Chanvillard G (2007) Experimental characterization of the self-healing of cracks in an ultra high performance cementitious material: Mechanical tests and acoustic emission analysis. Cem Concr Res 37(4):519–527

Ahn TH, Kishi T (2013) Crack Self-healing behavior of cementitious composites incorporating various mineral admixtures. J Adv Concr Technol 8(2):171–186.

Heap MJ, Lavallée Y, Laumann A, Hess KU, Meredith PG, Dingwell DB, Huismann S, Weise F (2013) The influence of thermal-stressing (up to 1000 °C) on the physical, mechanical, and chemical properties of siliceous-aggregate, high-strength concrete. Constr Build Mater 42:248–265.

Fukuda D, Nara Y, Kobayashi Y, Maruyama M, Koketsu M, Hayashi D, Ogawa H, Kaneko K (2012) Investigation of self-sealing in high-strength and ultra-low-permeability concrete in water using micro-focus X-ray CT. Cem Concr Res 42(11):1494–1500

Fukuda D, Nara Y, Hayashi D, Ogawa H, Kaneko K (2013) Influence of Fracture Width on Sealability in High-Strength and Ultra-Low-Permeability Concrete in Seawater. Materials 6(7):2578–2594

Gratier JP, Chen T, Hellmann R (1994) Pressure Solution as a Mechanism for Crack Sealing around Faults; SGS Open-file Report 94-228. Proc. Workshop LXIII on the Mechanical Involvement of Fluids in Faulting, CA, USA:279–300

Evans JP, Chester FM (1995) Fluid–rock interaction in faults of the San Andreas system: Inferences form San Gabriel fault rock geochemistry and microstructures. J Geophys Res 100(B7):13007–13020

Fisher DM, Brantley SL (1992) Models of quartz overgrowth and vein formation: Deformation and episodic fluid flow in an ancient subduction zone. J Geophys Res 97(B13):20043–20061

Tsang CF, Bernier F, Davies C (2005) Geohydromechanical processes in the excavation damaged zone in crystalline rock, rock salt, and indurated and plastic clays—In the context of radioactive waste disposal. Int J Rock Mech Min Sci 42(1):109–125

Graef BD, Cnudde V, Dick J, Belie ND, Jacobs P, Verstraete W (2005) A sensitivity study for the visualisation of bacterial weathering of concrete and stone with computerised X-ray microtomography. Sci Total Environ 341(1–3):173–183

Nara Y, Takada M, Mori D, Owada H, Yoneda T, Kaneko K (2010) Subcritical crack growth and long-term strength in rock and cementitious material. Int J Fract 164(1):57–71

Japan Society of Civil Engineers (2004) Recommendations for Design and Construction of Ultra High Strength Fiber Reinforced Concrete Structures—Draft [in Japanese]. Tokyo, Japan, Concrete Library 113:56–62

Hondros G (1959) The evaluation of poisson’s ratio and the modulus of materials of a low tensile resistance by the brazilian (indirect tensile) test with particular reference to concrete. Aust J Appl Sci 10(3):243–268

International Society for Rock Mechanics (1978) Commission on Standardization of Laboratory and Field Tests. Suggested Methods for Determining Tensile Strength of Rock Materials. Int J Rock Mech Min Sci Geomech Abstr 15:99–103

Mizukami M, Sakai H, Matsubaya O (1977) Na-Ca-Cl-SO4-type submarine formation waters at the seikan undersea tunnel, Japan. Chemical and isotopic documentation and its interpretation. Geochim Cosmochim Acta 41(9):1201–1212

Iwatsuki T, Furue R, Mie H, Ioka S, Mizuno T (2005) Hydrochemical baseline condition of groundwater at the Mizunami Underground Research Laboratory (MIU). Appl Geochem 20(12):2283–2302

Hama K, Kunimaru T, Metcalfe R, Martin AJ (2007) The hydrogeochemistry of argillaceous rock formations at the horonobe URL site, Japan. Phys Chem Earth 32(1–7): 170–180

Reed SJB (2010) Electron Microprobe Analysis and Scanning Electron Microscopy in Geology (2nd ed.). Cambridge University Press, UK

Kitamoto A (1999) A maximum likelihood thresholding methods considering the effect of mixels [in Japanese with English abstract]. Tech Rep IEICE PRMU99-166:7–14

Kitamoto A, Takagi M (1999) Image classification using probabilistic models that reflect the internal structure of mixels. Pattern Anal Appl 2:31–43.

Choi HS, Haynor DR, Kim Y (1991) Partial volume tissue classification of multichannel magnetic resonance images–A mixel model. IEEE Trans Med Imag 10(3): 395–407

Kato M, Takahashi M, Kawasaki S, Mukunoki T, Kaneko K (2013) Evaluation of porosity and its variation in porous materials using microfocus X-ray computed tomography considering the partial volume effect. Materials Transactions 54(9):1678–1685

Kato M, Takahashi M, Kawasaki S, Kaneko K (2014) Segmentation of multi-phase X-ray computed tomography images. Environmental Geotechnics. doi:10.1680/envgeo.13.00036

Title of Table

Table 1. Composition of high-strength and ultra-low-permeability concrete (HSULPC).

Table 2. Chemical composition of simulated seawater (mol l^{-1}) (following Fukuda et al. (2012; 2013)).

Figure captions

Fig. 1 Photograph of sealed HSULPC specimen after immersion in simulated seawater for 49 days.

Fig. 2 Photo of HSULPC specimen arrange for SEM/EDX observation. The new faces are prepared by cutting the specimen along the two faces indicated by red lines in Fig.1. Note that three squares in Fig. 2(c) indicate the observed areas in Figs. 3–8 mentioned in subsection 3.2.

Fig. 3 SEM image taken around the end of the macro-fractured HSULPC specimen sealed by precipitation.

Fig. 4 SEM image of the surface of one end of the macro-fractured HSULPC specimen.

Fig. 5 SEM image of macro-fracture in the interior of the specimen.

Fig. 6 Results of SEM/EDX analysis around the end of the macro-fractured HSULPC specimen sealed by precipitation. Note that cps indicates count per second.

Fig. 7 Results of SEM/EDX analysis on one end surface of the macro-fractured HSULPC specimen. Note that cps indicates count per second.

Fig. 8 Results of SEM/EDX analysis of macro-fracture in the interior of the specimen. Note that cps indicates count per second.

Fig. 9 Region of interest (ROI) for 3-D image analysis; (a) top view and (b) general view. In these X-rayCT images, brighter and darker colors correspond to regions with higher and lower densities, respectively.

Fig. 10 Binarized 3-D subtraction images between initial images and those obtained after immersion of specimen in simulated seawater for (a) 7 days, (b) 14 days and (c) 49 days. Only the images of the ROI in Fig. 9 are shown.

Fig. 11 Binarized subtraction images showing the same plane as that observed by SEM/EDX. The macro-fracture near the end surface of the specimen in this image corresponds to the region shown in Fig. 3.

Fig. 12 Relationship between percentage of sealing deposits, P_{seal}, and position, h, from the outermost surface of the ROI in the specimen immersed in simulated seawater for up to 49 days.

Fig. 13 Relationship between temporal change in percentage of sealing deposits, R_{seal}, and position, h, from the outermost surface of the ROI in the specimen immersed in simulated seawater for up to 49 days.

Tables

Table 1. Composition of high-strength and ultra-low-permeability concrete (HSULPC).

Composition	Amount [kg/m3]
Pre-mixed powder	2300 (Note) Following the recommendation proposed by Japan Society of Civil Engineers (2004), Low-heat Portland cement: 744–1014 Silica fume: 158–496 Fillers: 225–541 Aggregates: 631–947
Water-reducing admixture	24

Water	180

Table 2. Chemical composition of simulated seawater (mol l^{-1}) (following Fukuda et al. (2012; 2013)).

Ca^{2+}	SO_3^{2-}	Na^{+}	K^{+}	Cl^{-}	Mg^{2+}	HCO_3^{-}
10×10^{-3}	29×10^{-3}	45×10^{-2}	19×10^{-3}	56×10^{-2}	55×10^{-3}	24×10^{-4}

Figure 1
Click here to download high resolution image

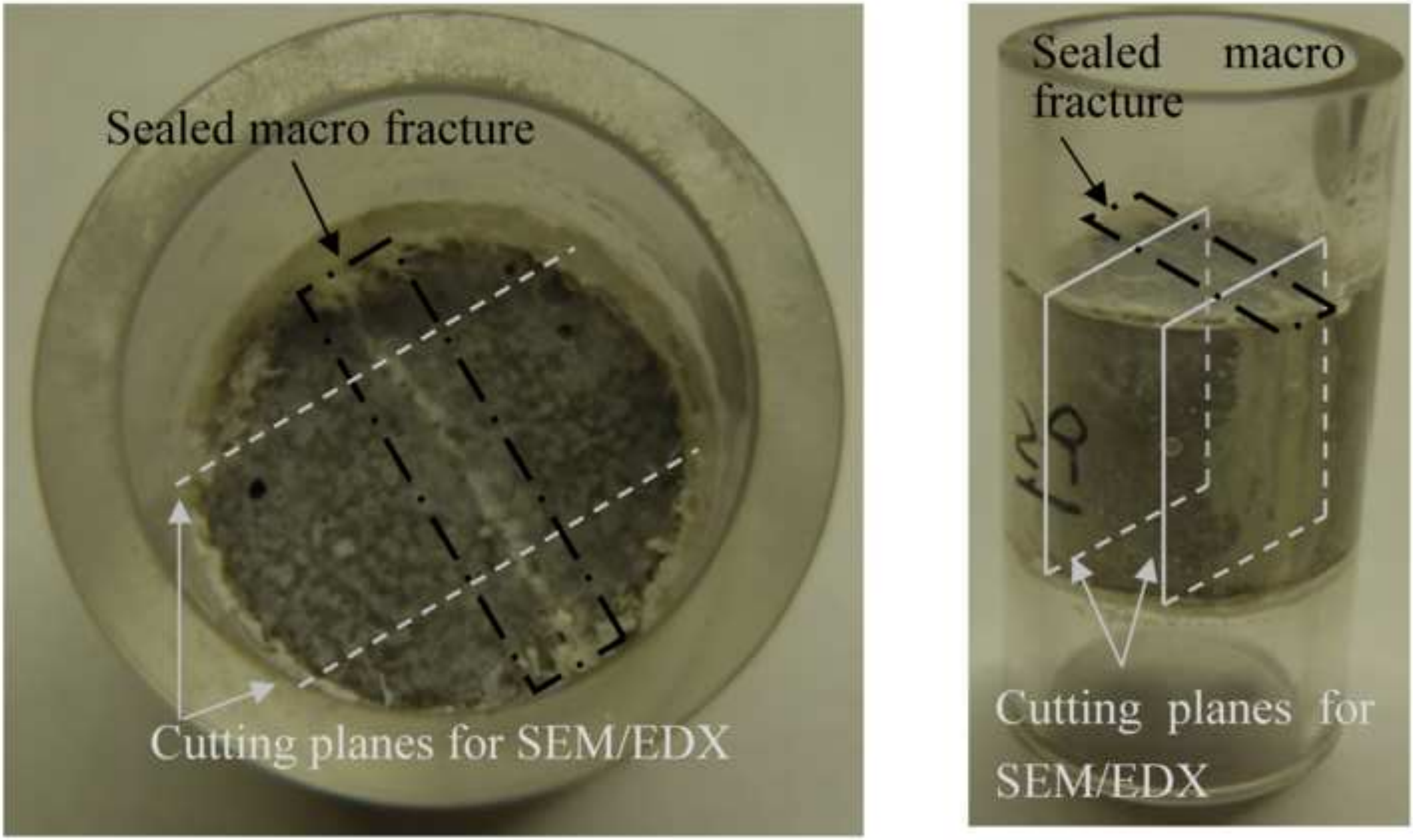

(a) Top view

(b) General view

Figure 2 Modified

Click here to download high resolution image

(a) Top view (b) General view (c) Observed surface

Figure 3
Click here to download high resolution image

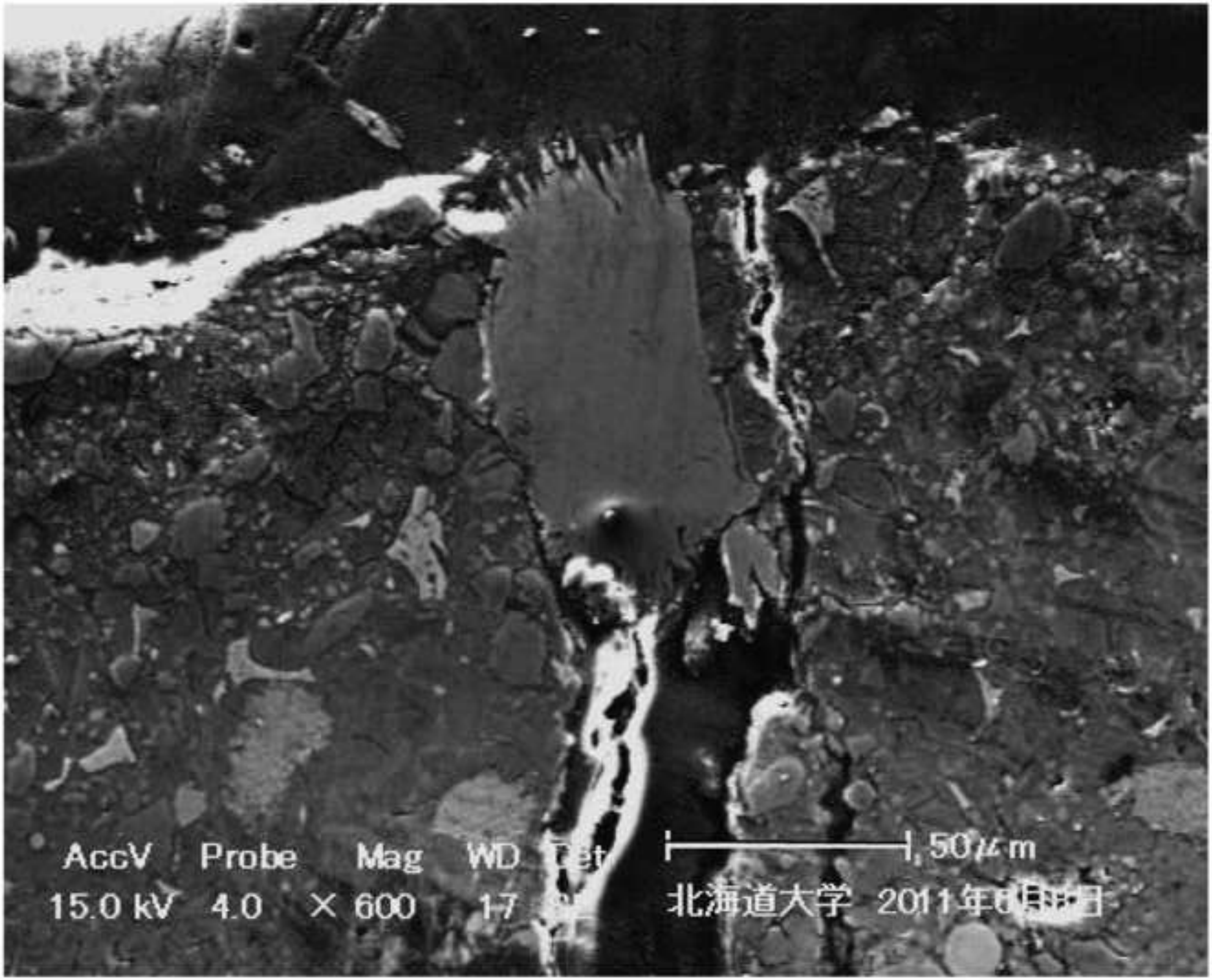

Figure 4

Click here to download high resolution image

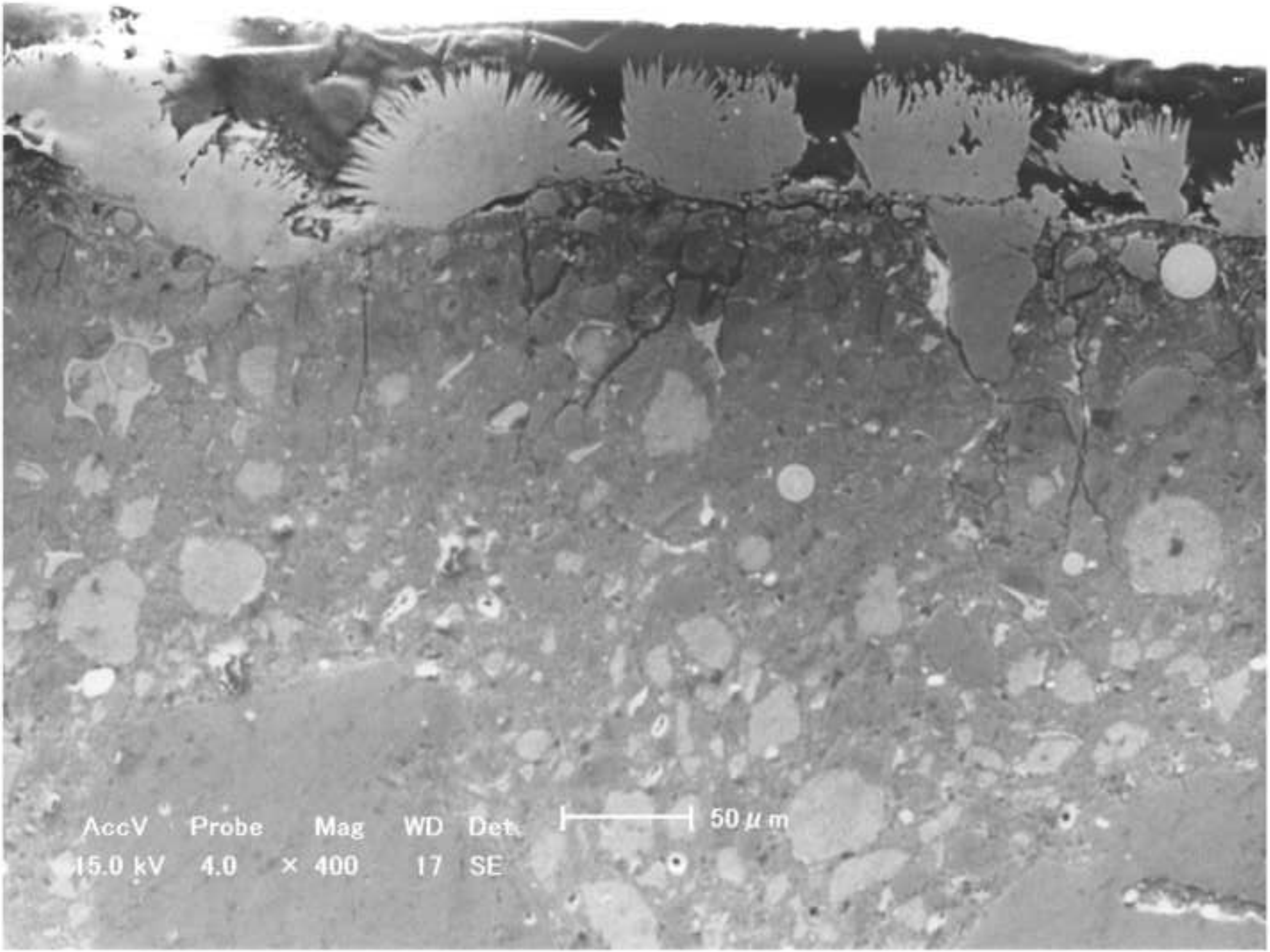

Figure 5

Click here to download high resolution image

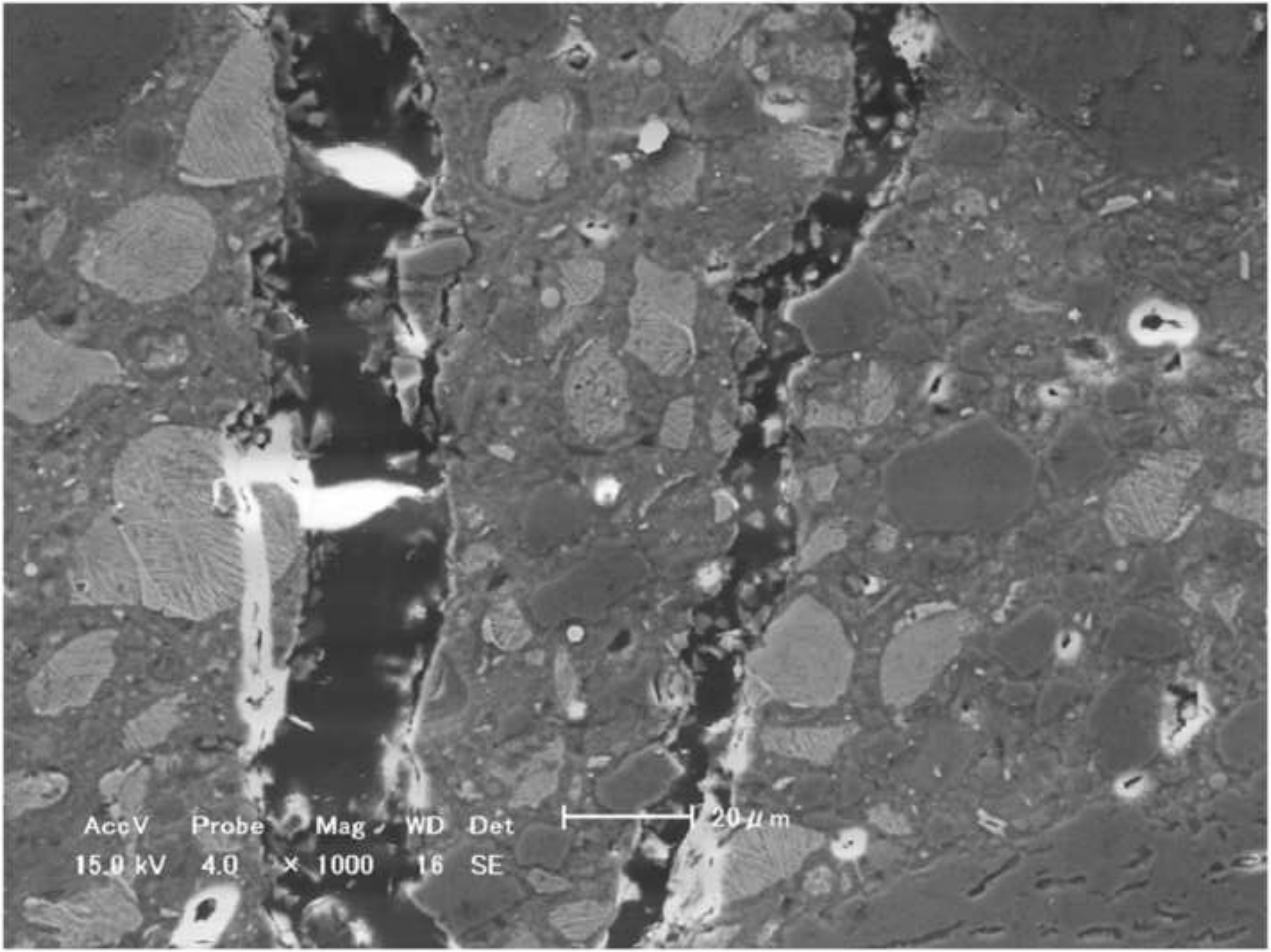

Figure 6 Modified

Click here to download high resolution image

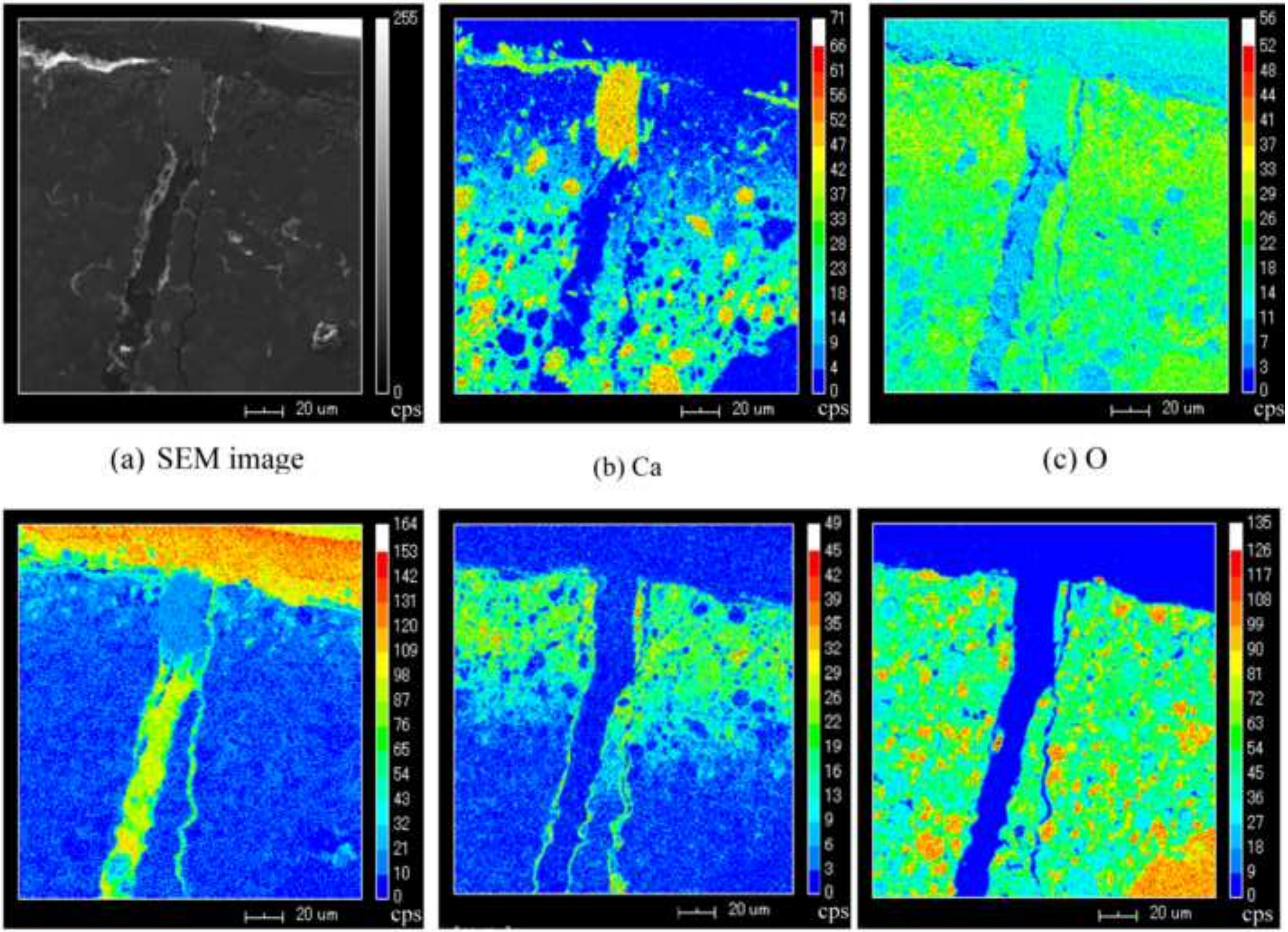

(a) SEM image (b) Ca (c) O

(d) C (e) Mg (f) Si

Figure 7 Modified
Click here to download high resolution image

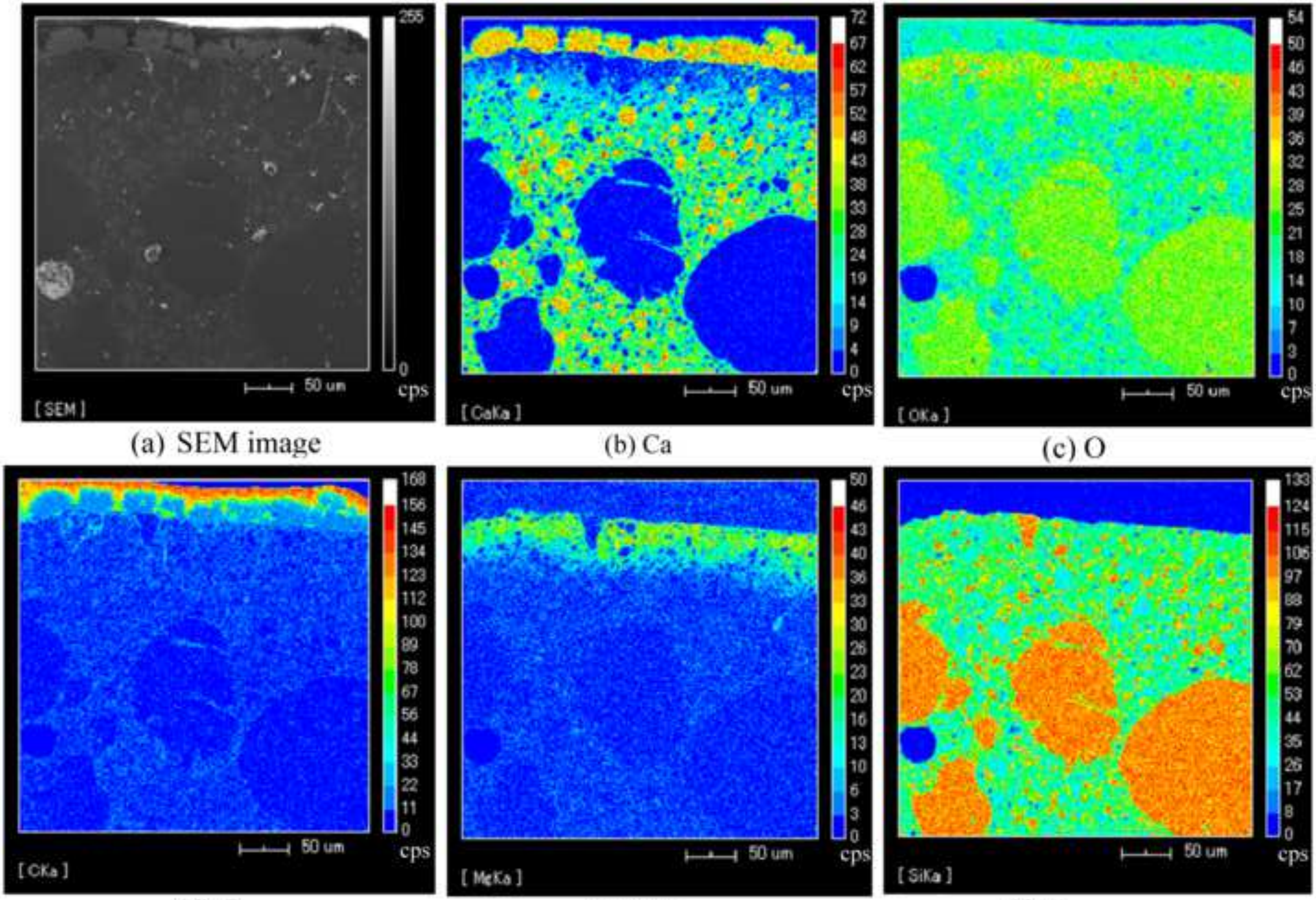

(a) SEM image (b) Ca (c) O
(d) C (e) Mg (f) Si

Figure 8 Modified

Click here to download high resolution image

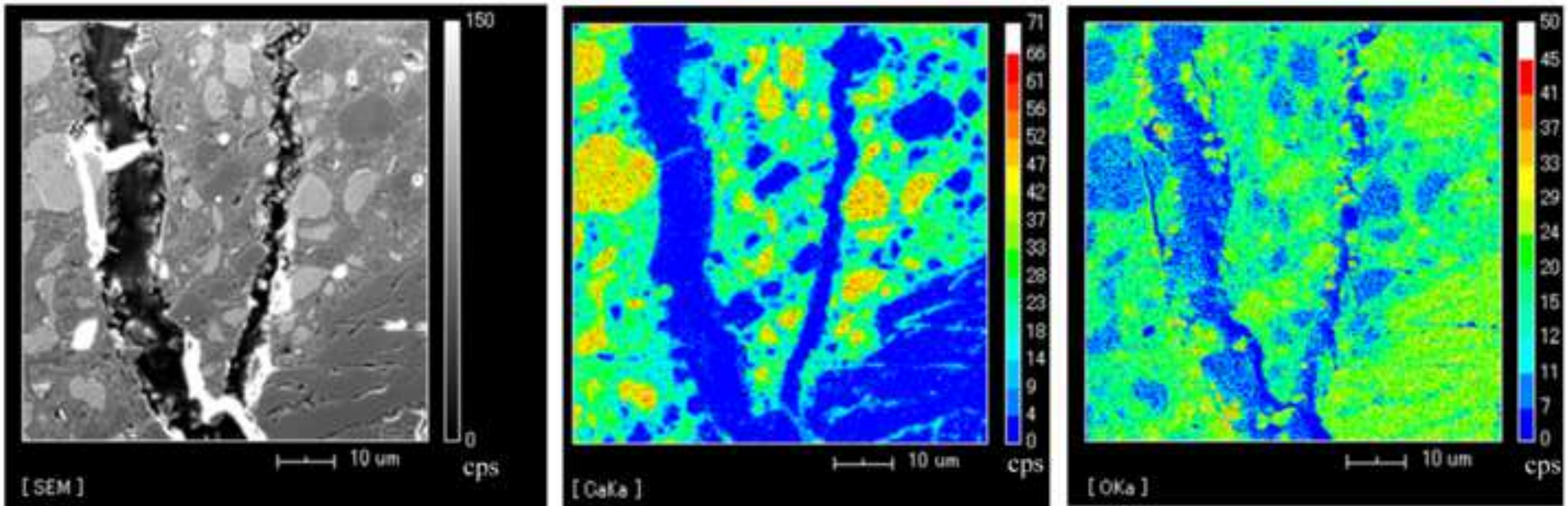

(a) SEM image (b) Ca (c) O

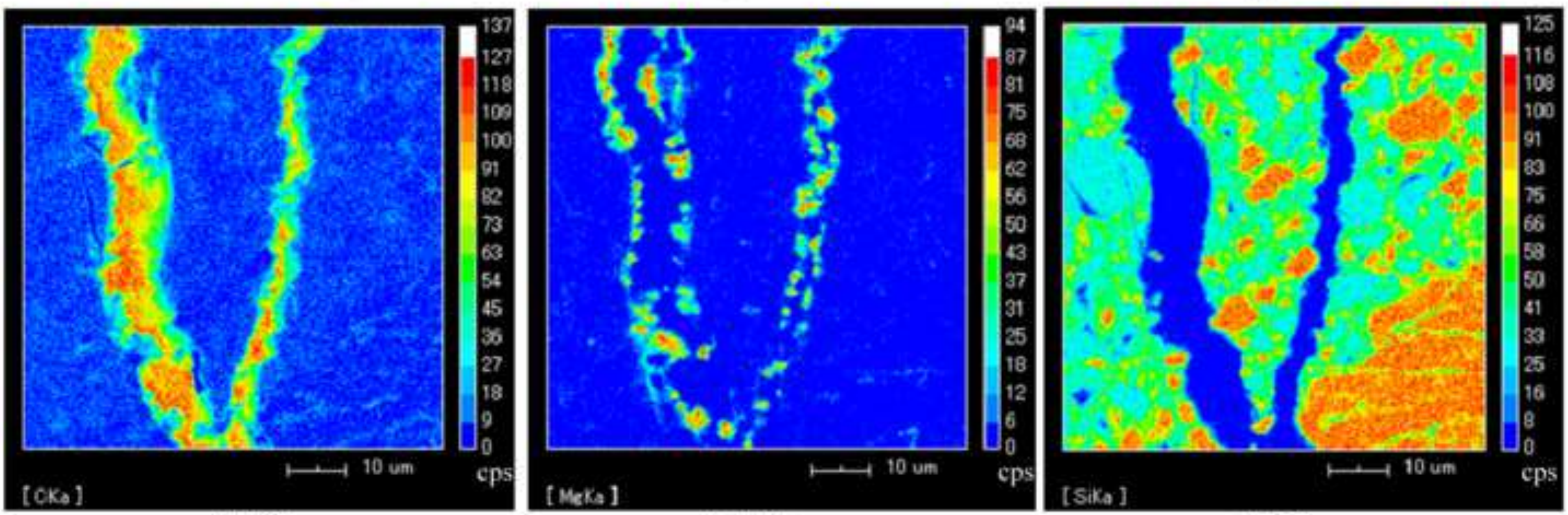

(d) C (e) Mg (f) Si

Figure 9
Click here to download high resolution image

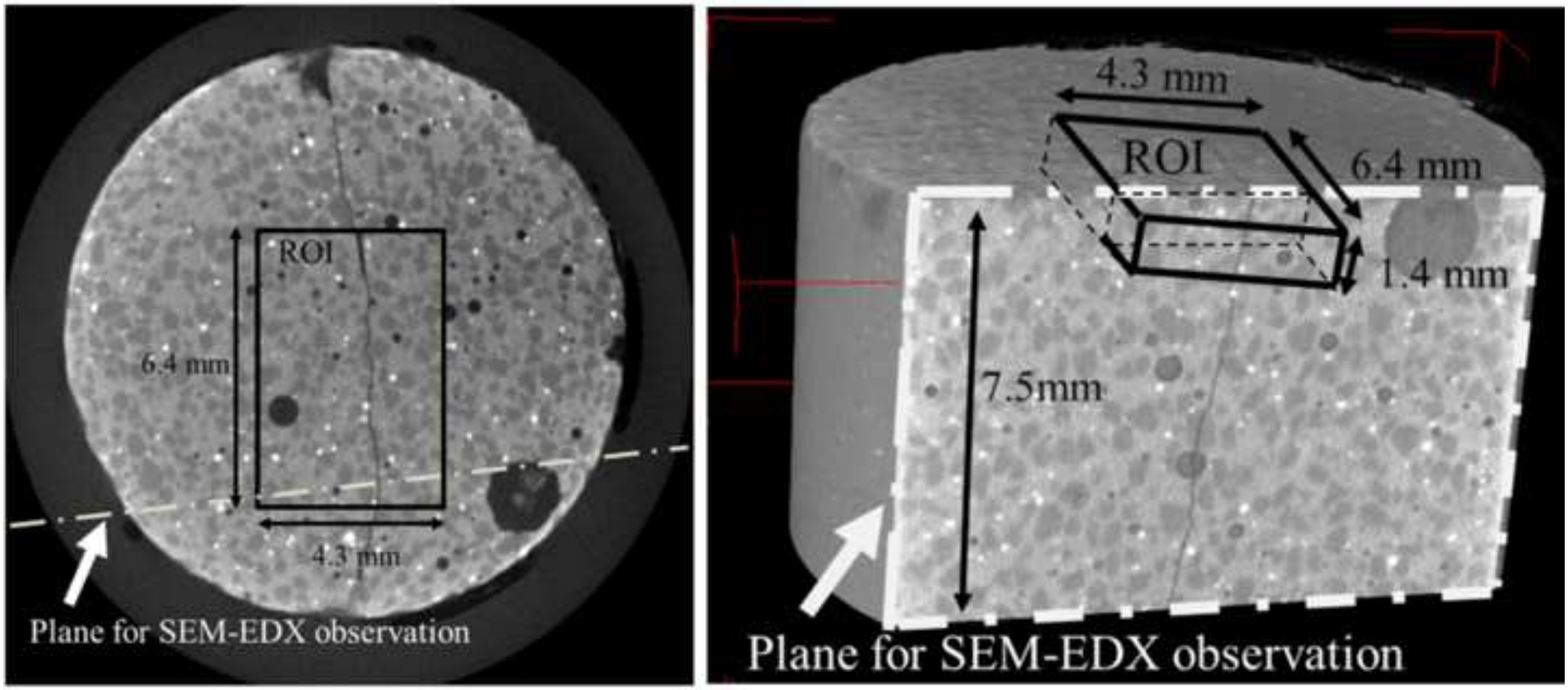

(a) (b)

Figure 10
Click here to download high resolution image

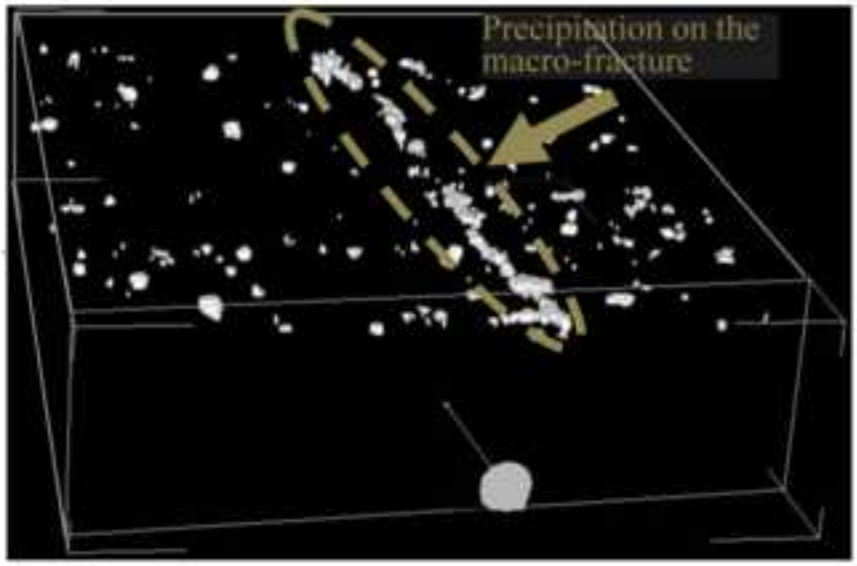

(a)

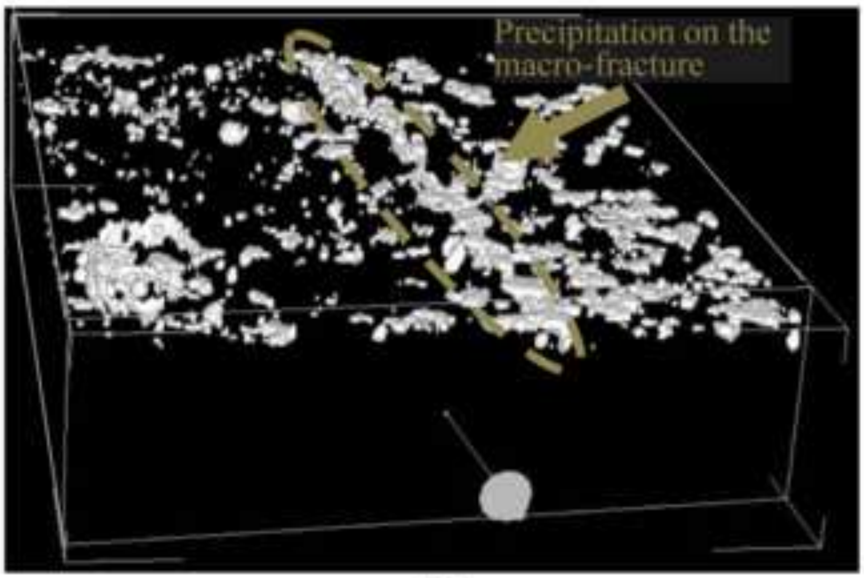

(b)

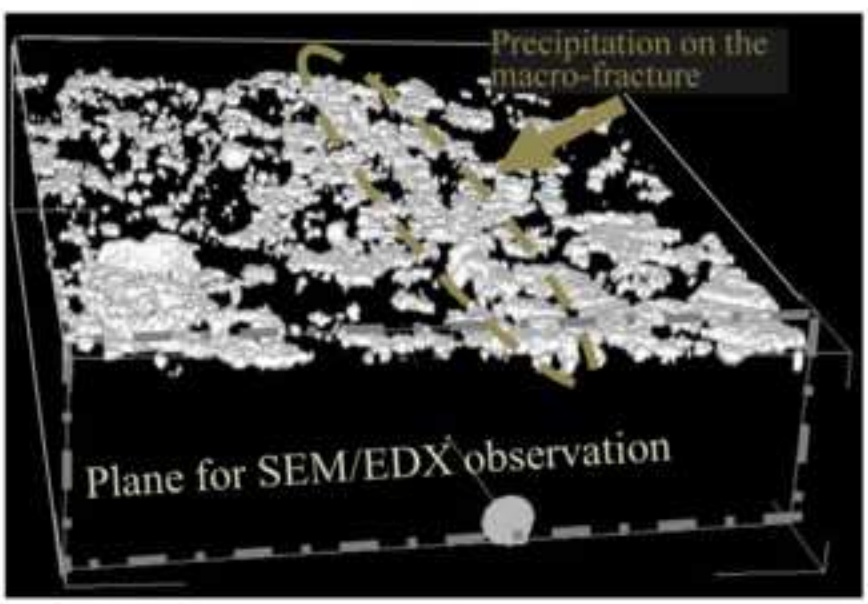

(c)

Figure 11
Click here to download high resolution image

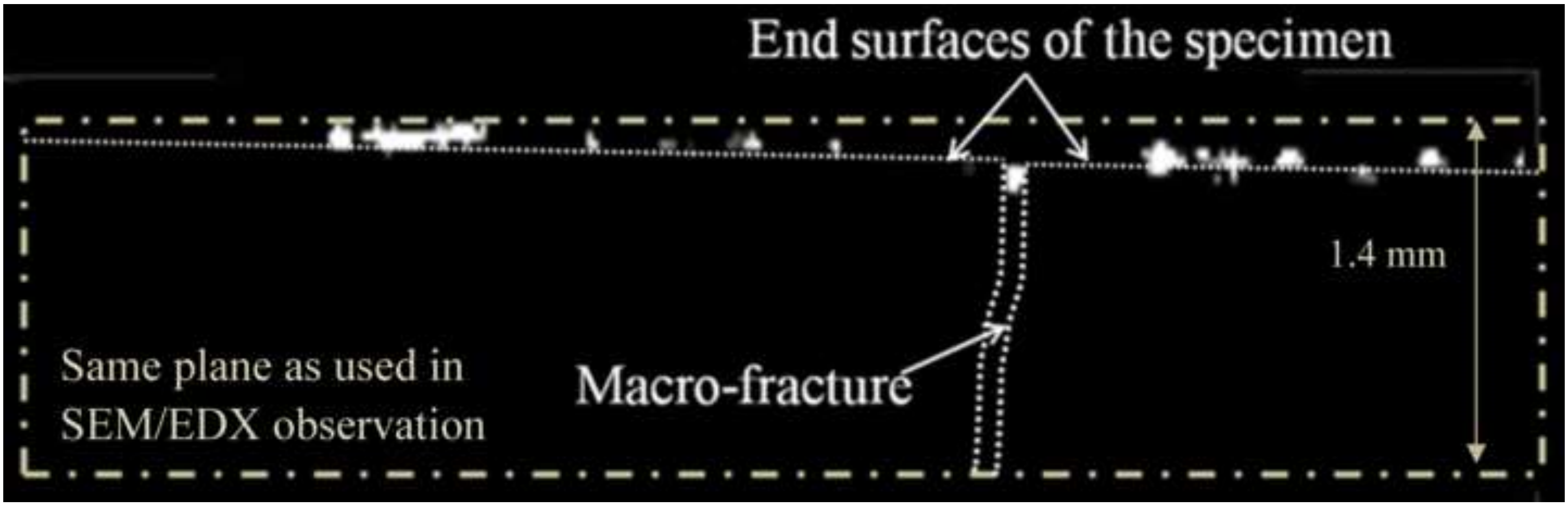

Figure 12
Click here to download high resolution image

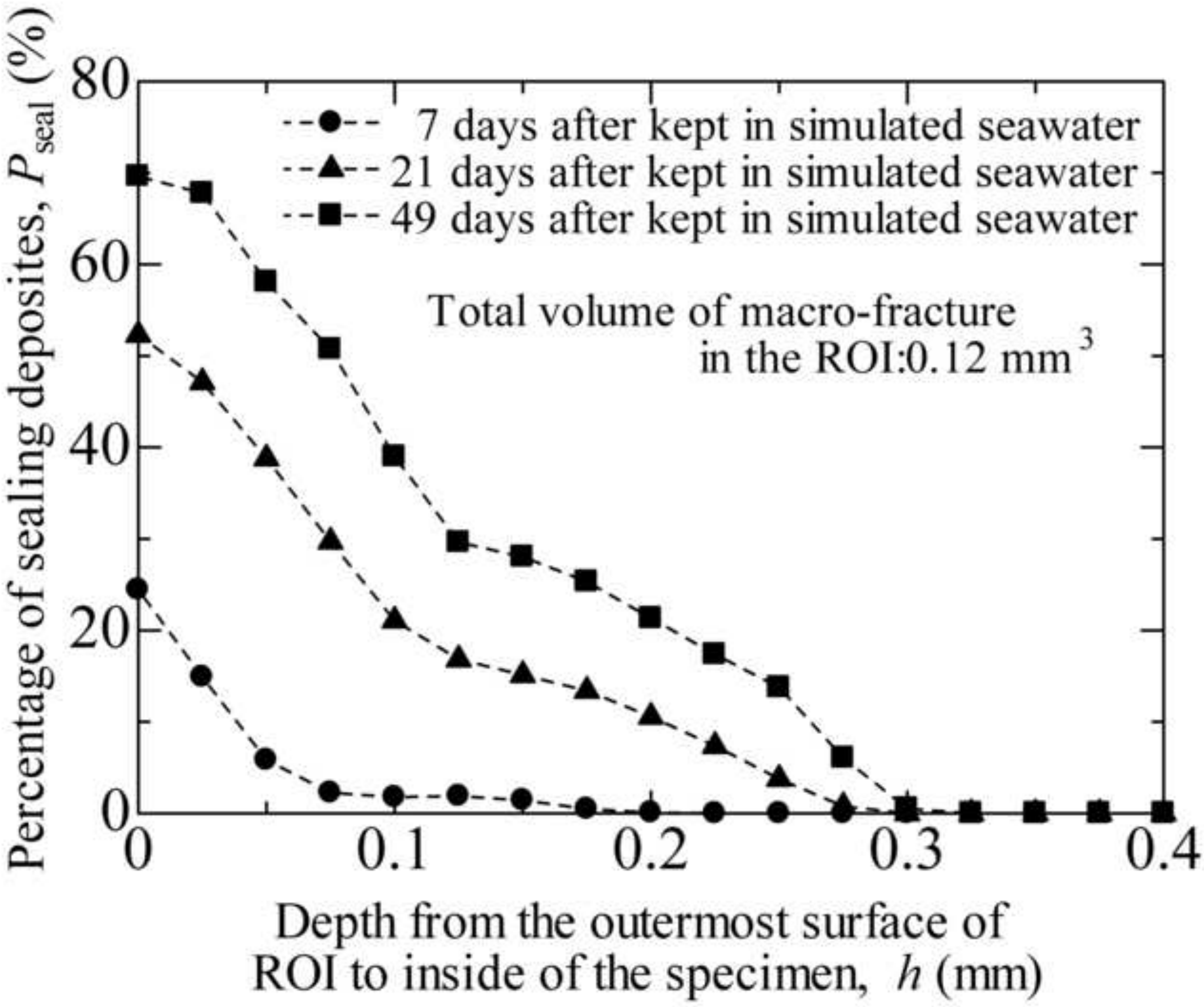

Figure 13
Click here to download high resolution image